A superconducting wireless energiser based on electromechanical energy conversion

Hongye Zhang [a,*], Tianhui Yang [b,*], Francesco Grilli [c], Wenxin Li [b], Paul M. Tuohy [a], Ying Xin [b]

[a] Department of Electrical and Electronic Engineering, The University of Manchester, Manchester M13 9PL, United Kingdom
[b] School of Electrical and Information Engineering, Tianjin University, Tianjin 300072, China
[c] Institute for Technical Physics, Karlsruhe Institute of Technology, Karlsruhe 76131, Germany

ARTICLE INFO

ABSTRACT

A superconducting magnet (SM) can produce high magnetic fields up to a dozen times stronger than those generated by an electromagnet made of normal conductors or a permanent magnet (PM), and thus has attracted increasing research efforts in many domains including medical devices, large scientific equipment, transport, energy storage, power systems, and electric machines. Wireless energisers, e.g., high temperature superconducting (HTS) flux pumps, can eliminate the thermal load from current leads and arc erosion of slip rings, and are thus considered a promising energisation tool for SMs. However, the time-averaged DC output voltage in existing HTS flux pumps is generated by dynamic resistance: the dynamic loss is unavoidable, and the total AC loss will become significant at high frequencies. This study introduces a highly efficient superconducting wireless energizer (SWE) designed specifically for SMs. The SWE takes advantage of the inherent properties of a superconducting loop, including flux conservation and zero DC resistivity. Extensive theoretical analysis, numerical modelling exploiting the $\mathbf{H}$-ϕ formulation, and experimental measurements were conducted to demonstrate the efficiency and efficacy of the novel SWE design. The electromechanical performance and loss characteristics of the SWE system have also been investigated. Compared to conventional HTS flux pumps, the proposed SWE has lower excitation loss, in the order of 10^{-1} mW, and thus can achieve a high system efficiency of no less than 95%. Furthermore, it has a simpler structure with higher reliability, considered ready for further industrial development. In addition to deepening the understating of the intricate electromechanical dynamics between magnetic dipoles and superconducting circuits, this article provides a novel wireless energisation technique for SMs and opens the way to step changes in future electric transport and energy sectors.

1. Introduction

Superconducting magnets (SMs) are capable of creating intense magnetic fields up to a dozen times greater than those produced by conventional electromagnets or permanent magnets (PMs) [1,2], and thus have a diverse range of applications, including medical devices (e.g., magnetic resonance imaging) [3], large scientific equipment (e.g., nuclear magnetic resonance, tokamaks, and particle accelerators) [4,5], transport (e.g., magnetic levitation) [6], energy storage (e.g., magnetic energy storage) [7,8], power systems (e.g., renewable power grids) [9,10], and electric machines (e.g., superconducting motors and generators) [11–13]. SMs need to operate with high transport currents, which makes the energisation of SMs a primary challenge.

In most cases, a static SM is powered through contact-type current leads made of ordinary metals which are connected to electronic power supplies [14]. However, the current leads carrying large cur-

rents have to work partially at room temperature and partially in the cryostat housing the SM. In this case, significant power dissipation can be generated, and a considerable thermal load is brought to the cryostat. Consequently, not only is the general efficiency of the cryogenic system decreased, but also the reliability and effectiveness of the SM are threatened by a possible quench. In addition, for a rotating SM, e.g., superconducting field windings embedded on the rotor of a superconducting machine, there exist additional challenges regarding the transfer of a larger direct current (DC) across a rotating joint. Currently, excitation methods employed include slip rings [15] and high-frequency brushless exciters [16,17]. However, slip rings are prone to arc erosion and mechanical wear, particularly at high current levels and rotational speeds [18]. While inductive brushless exciters offer a solution to circumvent direct electrical contacts, they come with drawbacks such as high costs, intricate structures, and the need for power

---

electronics to handle large DC currents, adversely affecting power density, reliability, and ease of maintenance [19,20].

To deal with the above-mentioned issues, wireless energisation techniques appear to be a superior option for SMs [21]. Superconducting flux pumps have emerged as a viable solution for compact wireless exciters, offering a promising alternative to traditional contact-type current leads, slip rings, and brushes [22–24]. These flux pumps can be classified into two categories: low temperature superconducting (LTS) and high temperature superconducting (HTS) flux pumps. LTS materials usually operate in liquid helium (typically at 4.2 K) because of their relatively lower critical temperatures. Since 1938, numerous electrically or mechanically driven LTS flux pumps have been designed and constructed, most of which achieve flux transfer via electric circuit switches by creating a normal-conducting region surrounded by the LTS material [25,26]. Compared to LTS materials, HTS ones have higher critical temperatures and critical currents and thus they are able to carry a larger current in the liquid nitrogen (LN$_2$) temperature range (typically at 77 K). As a result, the design difficulty and cost of cryogenic systems for HTS applications are less compared to LTS ones, making HTS flux pumps more promising [27]. However, the higher critical fields of HTS materials make it harder for them to generate normal-conducting zones needed for superconducting switches; therefore, HTS flux pumps have not been proposed until recent years. Existing HTS flux pumps can be classified into travelling wave and transformer-rectifier types. For both of them, the time-averaged DC output voltage is produced through a local rectification effect, which is induced by the presence of overcritical eddy currents flowing within the HTS layer characterised by dynamic resistance [28–32]. As a result, HTS flux pumps can act as a DC voltage source and pump currents to an external circuit. However, excitation power dissipation seems unavoidable in the utilised HTS coated conductors due to the occurrence of dynamic loss [33–35]. Consequently, as for the existing HTS flux pumps, two contradictory aspects have to be considered: on one hand, excessively low dynamic resistance leads to a low charging voltage level, resulting in an extended charging duration; on the other hand, if the dynamic resistance is excessively high, the substantial dynamic loss can compromise the efficiency of the flux pump system. A new HTS transformer-rectifier has been recently reported in [36] for energising HTS magnets. Despite the new mechanism making use of the screening currents in HTS coated conductors [36], the generation of resistance remains the basis of a charging voltage, the same as the other existing HTS flux pumps.

In order to energise SMs in a highly efficient and reliable way, a novel superconducting wireless energiser (SWE) has been presented in this paper. The proposed SWE has been conceived based on the electromechanical interaction between a moving magnetic dipole and a closed superconducting loop [37–40]. The mechanical energy from a moving PM undergoes conversion into electromagnetic energy subsequently stored in a SM by utilising the flux conservation property and zero DC resistivity of the superconducting loop. The effectiveness of the novel SWE has been validated by theoretical analysis, numerical modelling, and experimental measurements. The proposed SWE system is much simpler and more cost-effective compared to the existing HTS flux pumps, also without complicated power electronics. In addition, the generation of the DC does not rely on the creation of dynamic resistance in HTS coated conductors, and thus extremely low excitation losses can be expected. The proposed SWE is believed to provide a promising solution for advanced power conversion units in the electrical systems of transport applications.

2. Theoretical analyses

2.1. PM threading a superconducting loop

When a PM passes through a superconducting loop, an intriguing phenomenon reminiscent of "a violation of Lenz's law" emerges: the

mechanical force exerted on the PM does not consistently oppose its motion. In fact, throughout the entire movement process, the PM consistently experiences a repulsive force [37–40]. We have investigated the underlying cause of this peculiar electromechanical anomaly, which is attributed to the magnetic flux conservation of the superconducting loop dominated by its nearly zero resistivity [40]. Based on the preliminary theoretical research work in [40], the possibility of wirelessly energising a SM has been explored here. The diagram of the energy conversion system is illustrated in Fig. 1, in which a PM is initially positioned at the loop center, and then moves away from the superconducting loop along the z-axis.

The PM is modelled as a magnetic dipole characterised by a magnetic moment $\mathbf{m}$, with [41]

$$\mathbf{m} = \frac{1}{\mu_0}\mathbf{B_r}V$$

where μ_0 is the vacuum permeability, $\mathbf{B_r}$ denotes the remanence of the PM, and V devotes its volume.

In the local cylindrical coordinate system $o_m\text{-}\rho_m\varphi_m z_m$, at any given point in the space, the magnetic field distributions caused by the magnetic dipole can be calculated as [41]

$$B_{\rho_m}(r_m) = \frac{3\mu_0 m}{4\pi}\frac{\rho_{rm}z_{rm}}{\left(\rho_{rm}^2 + z_{rm}^2\right)^{5/2}} \tag{2}$$

$$B_{z_m}(r_m) = \frac{\mu_0}{4\pi}\left(\frac{3mz_{rm}^2}{r_m^5} - \frac{m}{r_m^3}\right) \tag{3}$$

where ρ_{rm} and z_{rm} are the positions of the studied point in the local coordinate system, and r_m stands for the distance between the magnetic dipole and the studied point.

In the cylindrical coordinate system $o\text{-}\rho\varphi z$, the position of the PM is noted as z_{PM}. As there is no current in the superconducting loop in the initial state, the magnetic flux within the loop is determined by the the area of the loop and the z-direction field component in the space generated by the PM. Therefore, the magnetic flux through the superconducting circuit can be written as
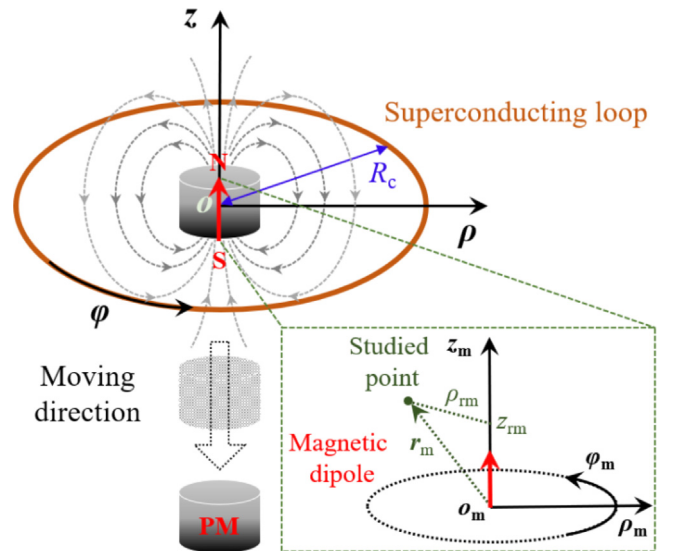

Fig. 1. Diagram of the superconducting wireless energisation system in the cylindrical coordinate system $o\text{-}\rho\varphi z$. R_c refers to the radius of the superconducting loop. The PM is initially situated at the loop center, with $z = 0$. The PM is characterized by a magnetic dipole, which is oriented in a local cylindrical coordinate system denoted as $o_m\text{-}\rho_m\varphi_m z_m$.

$$\begin{aligned}\Phi(z_{PM}) &= \int_0^{R_c} \frac{\mu_0}{4\pi}\left(\frac{3mz_{PM}^2}{r^5} - \frac{m}{r^3}\right)2\pi\rho d\rho \\ &= \frac{\mu_0 m}{2}\frac{R_c^2}{\left(R_c^2+z_{PM}^2\right)^{3/2}}\end{aligned} \quad (4)$$

where R_c is the radius of the superconducting loop.

In the initial stage, the PM is positioned at the center of the loop plane at room temperature, i.e., the conductive loop is not in a superconducting state. In this case, according to (4), the magnetic flux inside the loop can be written as

$$\Phi_0 = \frac{\mu_0 m}{2R_c} \quad (5)$$

Then, the conductive loop is cooled below the critical temperature to achieve superconductivity. According to the conservation of magnetic flux within a superconducting loop, the flux passing through the loop stay unchanged, regardless of the subsequent movement of the PM. For ease of analysis, the resistance of the superconducting loop is neglected here because of its dominant inductance. According to Faraday's law, we have [40]

$$-\frac{d\Phi}{dt} = L\frac{dI_{sc}}{dt} \quad (6)$$

where L stands for the inductance of the superconducting circuit, and I_{sc} represents the induced current in the loop. Eqs. (5) and (6) lead to

$$LI_{sc} + \Phi = \Phi_0 \quad (7)$$

Hence, the current induced in the superconducting loop resulting from the motion of the PM can be calculated as

$$I_{sc}(z_{PM}) = \frac{\Delta\Phi}{L} = \frac{\Phi_0 - \Phi}{L} = \frac{\mu_0 m}{2LR_c}\left[1 - \frac{R_c^3}{\left(R_c^2 + z_{PM}^2\right)^{3/2}}\right] \quad (8)$$

It can be inferred from (8) that the current induced in the superconducting loop is displacement-dependent, which is easy to understand in that the magnetic flux inside the loop directly relies on the distance between the PM and the loop plane. Nevertheless, when illustrating the changes in the induced current over time, it is necessary to take into account the velocity of the moving PM. In this case, the position of the PM in the cylindrical coordinate system is given by

$$z_{PM} = -\int vdt \quad (9)$$

and thus (8) can be transformed to

$$I_{sc}(t) = \frac{\mu_0 m}{2LR_c}\left\{1 - R_c^3\Big/\left[R_c^2 + \left(\int vdt\right)^2\right]^{3/2}\right\} \quad (10)$$

To reach the maximum current, the PM needs to move sufficiently far so that the second term in (8) and (10) can be neglected compared to 1. In this case, the maximum current is dependent on the maximum flux through the loop (i.e., the initial flux Φ_0) and its inductance, written as

$$I_{sc,\,max} = \frac{\Phi_0}{L} = \frac{\mu_0 m}{2LR_c} = \frac{B_r V}{2LR_c} \quad (11)$$

Based on the aforementioned theoretical analyses, it can be seen that the relative motion between a closed superconducting loop and a PM leads to the generation of a persistent DC within the loop, as depicted in equation (11). The magnitude of this persistent DC is influenced by various factors including the remanence and volume of the PM, as well as the inductance and radius of the superconducting loop. Consequently, the mechanical energy of a PM in motion can be effectively converted into electromagnetic energy, which is then stored within the superconducting loop. In other words, a SM can be wirelessly energised by a moving magnetic dipole, which constitutes the theoretical foundation of this paper.

Due to the energy conversion that happens between the PM and the superconducting loop, the loop actually does negative work to the PM, and vice versa. In accordance with Newton's third law, the mechanical force exerted on the PM by the superconducting loop is equivalent in magnitude to the force exerted on the loop by the PM. Therefore, the force experienced by the PM can be expressed as

$$\begin{aligned}F_{sc,PM}(z_{PM}) &= \int_0^{2\pi} I_{sc}B_\rho R_c d\varphi \\ &= 2\pi R_c \cdot \left\{\frac{\mu_0 m}{2LR_c}\left[1 - \frac{R_c^3}{\left(R_c^2+z_{PM}^2\right)^{3/2}}\right]\right\} \cdot \left[-\frac{3\mu_0 m}{4\pi}\frac{R_c z_{PM}}{\left(R_c^2+z_{PM}^2\right)^{5/2}}\right] \\ &= -\frac{3\mu_0^2 m^2 R_c}{4L}\frac{\left[\left(R_c^2+z_{PM}^2\right)^{3/2}-R_c^3\right]z_{PM}}{\left(R_c^2+z_{PM}^2\right)^4}\end{aligned} \quad (12)$$

where it should be noted that the negative sign comes from the transition of the radial field component from the coordinate system o_m-ρ_m-$\varphi_m z_m$ to o-$\rho\varphi z$, i.e., a negative sign has been introduced when incorporating (2) in (12) to correctly reflect the force direction when z_{PM} varies from zero to negative.

Accordingly, the time-varying mechanical force applied to the PM can be expressed as

$$F_{sc,PM}(t) = \frac{3\mu_0^2 m^2 R_c}{4L}\frac{\left\{\left[R_c^2 + \left(\int vdt\right)^2\right]^{3/2} - R_c^3\right\}\left(\int vdt\right)}{\left[R_c^2 + \left(\int vdt\right)^2\right]^4} \quad (13)$$

According to (8), the minimum and maximum induced currents occur at $z_{PM} = 0$ and $z_{PM} = -\infty$, respectively. The maximum changing rate of $I_{sc}(z_{PM})$ occurs when

$$\frac{d^2 I_{sc}}{dz_{PM}^2}\Big|_{z_{PM}=z_{sc,mcI}} = 0 \quad (14)$$

Therefore, through a series of calculations, it is obtained that

$$z_{sc,mcI} = -\frac{1}{2}R_c \quad (15)$$

and

$$\begin{aligned}I_{sc}(z_{sc,mcI}) &= \frac{\mu_0 m}{2LR_c}\left[1 - \frac{R_c^3}{\left(R_c^2+z_{sc,mI}^2\right)^{3/2}}\right] \\ &= \frac{\mu_0 m}{2LR_c}\left[1 - \frac{8}{5\sqrt{5}}\right] \\ &\approx 0.2845 I_{sc,max}\end{aligned} \quad (16)$$

Similarly, the PM experiences no forces at both $z_{PM} = 0$ and $z_{PM} = -\infty$, and thus the maximum value of $F_{sc,PM}(z_{PM})$ occurs when

$$\begin{cases}\frac{dF_{sc,PM}}{dz_{PM}}\Big|_{z_{PM}=z_{sc,mF}} = 0 \\ z_{sc,mF}\neq 0\end{cases} \quad (17)$$

On the basis of (12) and (17), it is obtained that

$$z_{sc,mF}\approx -0.8264R_c \quad (18)$$

and

$$\begin{aligned}F_{sc,PM}(z_{sc,mF}) &= -\frac{3\mu_0^2 m^2 R_c}{4L}\frac{\left[\left(R_c^2+z_{sc,mF}^2\right)^{3/2}-R_c^3\right]z_{sc,mF}}{\left(R_c^2+z_{sc,mF}^2\right)^4} \\ &\approx 0.0914\frac{\mu_0^2 m^2}{LR_c^3}\end{aligned} \quad (19)$$

In order to simplify the analysis, the velocity of the PM is considered as a constant, with $v = v_c$. Then, (10) and (13) can be simplified as

$$I_{sc}(t) = \frac{\mu_0 m}{2LR_c}\left[1 - \frac{R_c^3}{\left(R_c^2 + v_c^2 t^2\right)^{3/2}}\right] \quad (20)$$

$$F_{sc,PM}(t) = \frac{3\mu_0^2 m^2 R_c v_c}{4L}\frac{\left[\left(R_c^2 + v_c^2 t^2\right)^{3/2} - R_c^3\right]t}{\left(R_c^2 + v_c^2 t^2\right)^4} \quad (21)$$

H. Zhang et al.

Superconductivity 7 (2023) 100057

Accordingly, $t_{\text{sc,mcI}}$ and $t_{\text{sc,mF}}$ are defined to characterise the moments when the maximum changing rate of the induced current and the maximum force exerted on the PM occur, respectively, with

$$t_{\text{sc,mcI}} = \frac{R_c}{2v_c} \tag{22}$$

$$t_{\text{sc,mF}} \approx 0.8264 \frac{R_c}{v_c} \tag{23}$$

$z_{\text{sc,mcI}}$, $z_{\text{sc,mF}}$, $t_{\text{sc,mcI}}$ and $t_{\text{sc,mF}}$ will be employed to validate the derived equations in this study by comparing them with numerical simulations and experimental results. In summary, the mechanical energy of the moving PM can be effectively converted into electromagnetic energy, which is stored within the superconducting loop in the form of a persistent circulating current represented by $I_{\text{sc,max}}$.

2.2. PM threading a normal conductive loop

To better illustrate the distinctions between a superconducting loop and a conventional conductive loop, the explicit formulae to describe the electromagnetic behaviour of a normal conductive loop passed through by a PM has also been studied. It is assumed that the inductance of a normal conductive loop can be neglected compared to its dominant resistance. As a result, according to Faraday's law, it is obtained that

$$I_{\text{nc}} = -\frac{1}{R}\frac{d\Phi}{dt} \tag{24}$$

where R represents the resistance of the normal conductive loop. It can be seen from (24), different from (6), that the induced current I_{nc} relies on the the rate of change of the magnetic flux within the loop. It is known from (4) that the magnetic flux is z_{PM}-dependent; hence, the induced current depends on dz_{PM}/dt, namely the velocity of the PM. Therefore, we obtain

$$I_{\text{nc}}(z_{\text{PM}}) = -\frac{1}{R}\frac{d\Phi}{dz_{\text{PM}}}\frac{dz_{\text{PM}}}{dt} = -\frac{3\mu_0 m}{2R}\frac{R_c^2 z_{\text{PM}}}{\left(R_c^2 + z_{\text{PM}}^2\right)^{5/2}}v \tag{25}$$

Accordingly, the force imparted on the PM by the current induced in the normal conductive loop can be calculated by

$$
\begin{aligned}
F_{\text{nc,PM}}(z_{\text{PM}}) &= 2\pi R_c I_{\text{nc}} B_\rho \\
&= 2\pi R_c \cdot \left[-\frac{3\mu_0 m}{2R}\frac{R_c^2 z_{\text{PM}}}{\left(R_c^2 + z_{\text{PM}}^2\right)^{5/2}}v \right] \cdot \left[-\frac{3\mu_0 m}{4\pi}\frac{R_c z_{\text{PM}}}{\left(R_c^2 + z_{\text{PM}}^2\right)^{5/2}} \right] \\
&= \frac{9\mu_0^2 m^2}{4R}\frac{R_c^4 z_{\text{PM}}^2}{\left(R_c^2 + z_{\text{PM}}^2\right)^5}v
\end{aligned} \tag{26}
$$

According to (25), in a normal conductive loop, the induced current is found to be zero at both $z_{\text{PM}} = 0$ and $z_{\text{PM}} = -\infty$. Therefore, the normal conductive loop is not capable of storing energy after the entire dynamic process because of the energy dissipation due to resistance. Designating $z_{\text{nc,mI}}$ as the position of the PM where the maximum induced current appears, we have

$$\frac{dI_{\text{nc}}}{dz_{\text{PM}}}\Big|_{z_{\text{PM}} = z_{\text{nc,mI}}} = 0 \tag{27}$$

Based on (25) and (27), it is obtained that

$$z_{\text{nc,mI}} = -\frac{1}{2}R_c \tag{28}$$

and

$$I_{\text{nc}}(z_{\text{nc,mI}}) = \frac{3\mu_0 m v_c}{4R}\frac{32}{25\sqrt{5}R_c^2} \approx 0.4293\frac{\mu_0 m v_c}{R R_c^2} \tag{29}$$

Comparing (15) and (28), it can be concluded that when a PM passes through both a superconducting loop and a normal conductive loop with identical geometries, the maximum current induced in the

normal conductive loop exactly occurs at the PM position where the maximum current changing rate of the current induced in the superconducting loop happens.

Similarly, if we note $z_{\text{nc,mF}}$ as the PM position where the maximum force applied to the PM occurs, we obtain

$$\begin{cases} \frac{dF_{\text{nc,PM}}}{dz_{\text{PM}}}\Big|_{z_{\text{PM}} = z_{\text{nc,mF}}} = 0 \\ z_{\text{nc,mF}} \neq 0 \end{cases} \tag{30}$$

Then, we can obtain

$$z_{\text{nc,mF}} = -\frac{1}{2}R_c \tag{31}$$

and

$$F_{\text{nc,PM}}(z_{\text{nc,mF}}) = \frac{9\mu_0^2 m^2 v_c}{16R R_c^4}\frac{1024}{3125} \approx 0.1843\frac{\mu_0^2 m^2 v_c}{R R_c^4} \tag{32}$$

Comparing (28) and (31), it can be observed that in a normal conductive loop, the maximum induced current and the force imparted on the PM occur at the same position of the PM. However, this is not the case for a superconducting loop, as demonstrated by equations (15) and (18). Hence, the electromechanical interactions between a PM and a superconducting loop exhibit distinct differences compared to a normal conducting system.

In the time domain, based on (9), (25) and (26) can be transformed into

$$I_{\text{nc}}(t) = \frac{3\mu_0 m}{2R}\frac{R_c^2 \int v\,dt}{\left[R_c^2 + \left(\int v\,dt\right)^2\right]^{5/2}}v \tag{33}$$

$$F_{\text{nc,PM}}(t) = \frac{9\mu_0^2 m^2}{4R}\frac{R_c^4 \left(\int v\,dt\right)^2}{\left[R_c^2 + \left(\int v\,dt\right)^2\right]^5}v \tag{34}$$

In the case of a constant PM velocity with $v = v_c$, (33) and (34) can be rewritten as

$$I_{\text{nc}}(t) = \frac{3\mu_0 m}{2R}\frac{R_c^2 v_c^2 t}{\left(R_c^2 + v_c^2 t^2\right)^{5/2}} \tag{35}$$

$$F_{\text{nc,PM}}(t) = \frac{9\mu_0^2 m^2}{4R}\frac{R_c^4 v_c^3 t^2}{\left(R_c^2 + v_c^2 t^2\right)^5} \tag{36}$$

$t_{\text{nc,mI}}$ and $t_{\text{nc,mF}}$ are defined to separately characterise the moments when the maximum current induced in the normal conductive loop and the maximum force applied to the PM occur, and thus it is obtained that

$$t_{\text{nc,mI}} = t_{\text{nc,mF}} = \frac{R_c}{2v_c} \tag{37}$$

2.3. Comparison between the two systems

In this section, we will consider a PM with a height of 20 mm, a radius of 10 mm, and the remanent flux density $B_r = 1$ T, a superconducting loop ($R = 0$) with $R_c = 50$ mm and $L = 5$ μH, as well as a conductive loop with $R_c = 50$ mm and $R = 1$ Ω. The velocity of the PM is chosen as $v_c = 10$ mm/s. On the basis of (20), (21), (31), and (32), the time-domain variation of the currents induced in the two conductive loops and the forces exerted on the PM by the two different loops are presented together in Fig. 2. It should be noted that the currents and forces have been standardised by normalising them to their maximum values for better illustration (though I_{sc} and $F_{\text{sc,PM}}$ are far greater than I_{nc} and $F_{\text{nc,PM}}$).

It can be seen from Fig. 2 that $t_{\text{sc,mcI}}$, $t_{\text{sc,mF}}$, $t_{\text{nc,mI}}$, and $t_{\text{nc,mF}}$ calculated by (22), (23), and (37) demonstrate a strong agreement with the waveforms of currents and forces. Additionally, Fig. 2 clearly exhi-
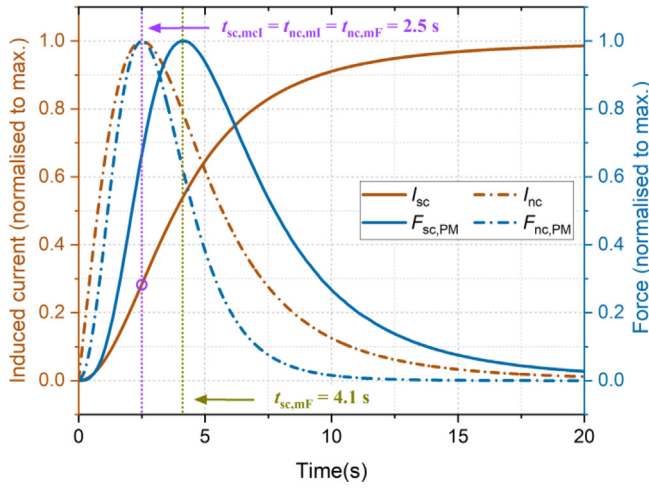
Fig. 2. Normalised currents induced in both a superconducting loop and a normal conductive loop, as well as the normalised forces imparted on the PM in both scenarios. $B_r = 1$ T, $R_c = 50$ mm, $L = 5$ μH, $R = 1$ Ω, and $V_c = 10$ mm/s.

bits the discrepancy in electromechanical behaviours between a superconducting and a normal conductive system. It can be seen that with the PM moving away from the initial position, the current generated in the superconducting loop is approaching the maximum value, $I_{sc,max}$, which is determined by Eq. (11). Under ideal circumstances, once the PM has moved a sufficient distance, the induced DC approaching $I_{sc,max}$ will circulate permanently in the superconducting loop. As a result, the mechanical energy of a PM can be converted to electromagnetic energy stored in a superconducting circuit.

It is important to highlight that the focus in this analysis is specifically on the scenario where the magnetic flux introduced by a PM to a conductive loop diminishes gradually. In this context, Lenz's law remains applicable to characterise the electromechanical behavior of both normal conductive and superconducting systems. Accordingly, the induced current generated in response to the changing magnetic flux acts to oppose that change, resulting in a mechanical force that counteracts the motion of the PM.

2.4. PM threading a superconducting SM

In practical applications, a SM is usually in the form of a superconducting coil composed of many turns. Considering a superconducting coil of N turns with the self-inductance of L_{tot}, the current induced in each coil turn, I_t, can be calculated in the time domain as

$$I_t(t) = \frac{\mu_0 m}{2N} \sum_{k=1}^{N} \frac{1}{L_k R_{c,k}} \left\{ 1 - \frac{R_{c,k}^3}{\left[R_{c,k}^2 + \left(\int v dt \right)^2 \right]^{3/2}} \right\} \tag{38}$$

where $R_{c,k}$ and L_k represent the radius and the self-inductance of the k-th turn in the coil. Given that the current induced in each turn is the same, according to (8), it can be concluded that L_k is proportional to the flux change through the k-th turn, i.e.,

$$\begin{cases} \sum_{k=1}^{N} L_k = L_{tot} \\ \frac{\Delta \Phi_j}{L_j} = \frac{\Delta \Phi_{j+1}}{L_{j+1}} \end{cases} \tag{39}$$

where $j \in [1, N-1]$.

Accordingly, the force applied to the PM by the N-turn SM can be written as

$$F_{tot}(t) = \frac{3\mu_0^2 m^2 \left(\int v dt \right)}{4} \sum_{k=1}^{N} \frac{R_{c,k}}{L_k} \frac{\left\{ \left[R_{c,k}^2 + \left(\int v dt \right)^2 \right]^{3/2} - R_{c,k}^3 \right\}}{\left[R_{c,k}^2 + \left(\int v dt \right)^2 \right]^4} \tag{40}$$

On the basis of Sections 2.1, 2.2, and 2.3, by replacing $\int v dt$ in (38) and (40) with z_{PM}, we can obtain the generated current and the force experienced by the PM in the space domain, noted as $I_t(z_{PM})$ and $F_{tot}(z_{PM})$, respectively. In the case of constant PM velocity with $v = V_c$, $\int v dt$ will be replaced by $V_c t$.

Based on (11), the maximum permanent DC that can be induced in each turn of the SM can be approximated as

$$I_{t,max} \approx N \frac{\mu_0 m}{2L_{tot} R_{c,avg}} \tag{41}$$

where $R_{c,avg}$ is the average radius of the SM determined by its inner radius R_i and outer radius R_o, with $R_{c,avg} = (R_i + R_o)/2$. Consequently, the electromagnetic energy stored in the SM is calculated by

$$W_{em} = \frac{L_{tot} I_t^2(t)}{2} \tag{42}$$

with the maximum value

$$W_{em,max} = \frac{L_{tot} I_{t,max}^2}{2} = \frac{N^2 \mu_0^2 m^2}{8 L_{tot} R_{c,avg}^2} \tag{43}$$

The input mechanical energy of the whole system can be calculated as

$$W_{mec} = \int_0^t F_{tot}(t) v dt \tag{44}$$

and thus the system efficiency can be quantified as

$$\eta = \frac{W_{em}}{W_{mec}} \tag{45}$$

3. Modelling and experiment methodology

In order to verify the derived formulae presented in Section 2, the finite element method (FEM) based numerical modelling technique and experimental measurements have been adopted.

Two different types of PMs and a SM fabricated from a double pancake HTS coil have been utilised, of which the specifications are shown in Table 1. In terms of the SWE system, the objective is to achieve the most current induced in the HTS coil while optimising the overall system efficiency. Therefore, the moving velocity of the PM should be kept sufficiently low to avoid generating high AC loss in the HTS coil due to high-frequency fields [42–44].

3.1. H-ϕ formulation based numerical model

The magnetic field, **H**, and the magnetic scalar potential, ϕ, have been coupled together as the **H**-ϕ formulation [35] to solve Maxwell's

Table 1
PM and HTS coil Parameters.

Symbols	Parameter	Value
R_{PM-1}	Radius of PM-1	12.5 mm
R_{PM-2}	Radius of PM-2	10 mm
h	Height of PM-1 & PM-2	20 mm
V_1	Volume of the PM-1	3125π mm³
V_2	Volume of the PM-2	2000π mm³
B_{r1}	Remanence of the PM-1	1.40 T
B_{r2}	Remanence of the PM-2	1.43 T
V_c	PM velocity	3.5 mm/s
μ_0	Free space permeability	$4\pi \times 10^{-7}$ H/m
R_o	Outer radius of the SM	36.4 mm
R_i	Inner radius of the SM	30.4 mm
I_{c0}	Self-field critical current @ 77 K	110 A
W	Bi-2223 tape width	4.2 mm
N	Turn number of the HTS coil	44
L	HTS coil inductance	0.2 mH

equations based on FEM: as demonstrated in Fig. 3, the full vector **H** is solved in the superconducting region and the air domain surrounding it (**H**-solved region); the magnetic scalar potential ϕ is calculated in the PM region and the current-free air surrounding it (ϕ-solved region). The combination of the **H**- and ϕ-formulations can effectively decrease the number of degrees of freedom and mitigate the computational complexity [45]. In view of the symmetric structure of the studied wireless energisation system, it can be simulated with a 2D axisymmetric model in a cylindrical coordinate system $o\text{-}\rho\varphi z$. In the **H**-solved region, applying Faraday's law and the constitutive law, we derive

$$\begin{bmatrix} -\frac{\partial E_\varphi}{\partial z} \\ \frac{1}{\rho}\frac{\partial(\rho E_\varphi)}{\partial \rho} \end{bmatrix} = -\mu_0\mu_r \begin{bmatrix} \frac{\partial H_\rho}{\partial t} \\ \frac{\partial H_z}{\partial t} \end{bmatrix} \tag{46}$$

where E and H separately represent the electric field and magnetic field strength, and μ_r refers to the relative permeability of the studied region.

Ampere's law is utilised to calculate the current density in the superconducting loop, resulting in

$$J_\varphi = \frac{\partial H_\rho}{\partial z} - \frac{\partial H_z}{\partial \rho} \tag{47}$$

As far as a superconductor is concerned, its resistivity is characterised by the **E-J** power law [46], as

$$|E_\varphi| = E_0 \left[\frac{|J_\varphi|}{J_c(\mathbf{H})} \right]^n \tag{48}$$

where E_0 denotes the characteristic electric field, with $E_0 = 10^{-4}$ V/m; n is the power law constant, with $n = 21$ here; and $J_c(\mathbf{H})$ stands for the magnetic field dependence of the critical current of the HTS material, determined by [47]

$$J_c(\mathbf{H}) = \frac{J_{c0}}{\left(1 + \sqrt{k^2 H_\parallel^2 + H^2/H_0}\right)^\alpha} \tag{49}$$

where J_{c0} is the fitted critical current density of the superconducting layer at zero external magnetic fields; H_0 represents the characteristic magnetic field strength constant, with $H_0 = 81.965$ kA/m for the studied HTS tape; $H_\perp$ (H_r in the studied case) and $H_\parallel$ (H_z in the studied case) denote the field components aligned perpendicular and parallel to the broad surface of the HTS tape, respectively; k and α are both fitting parameters, with $k = 0.061$, and $\alpha = 0.76$.

Given that the skin effect can be neglected on account of the low moving speed of the PM, the homogenization approach proposed in
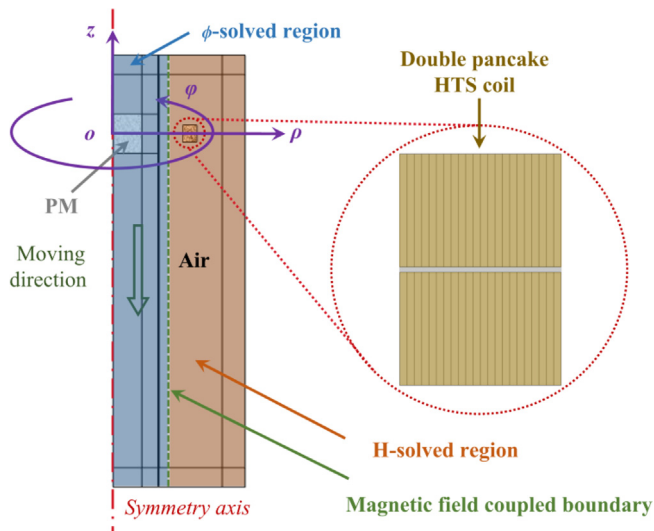
[48,49] has been applied to each coil turn so as to further reduce the computational complexity. Hence, the equivalent field dependence of the critical current density, $J_{c,eq}(\mathbf{H})$, can be written as

$$J_{c,eq}(\mathbf{H}) = J_c(\mathbf{H}) \cdot f_{sc} \tag{50}$$

where f_{sc} represents the fill factor characterising the extent of the HTS layer within a whole tape structure (a HTS tape consists of the HTS layer, non-superconducting tape layers, as well as the inevitable air gap). Therefore, considering the geometries of the chosen Bi-2223 coil, the self-field critical current density is $J_{c0,eq} = J_{c0} \cdot f_{sc} = 2 \times 10^8$ A/m².

Combining (46)–(50), the **H**-formulation based governing equation can be obtained as

$$\begin{bmatrix} -\frac{\partial\left\{E_0\left[\left(\frac{\partial H_\rho}{\partial z} - \frac{\partial H_z}{\partial \rho}\right)/J_{c,eq}(\mathbf{H})\right]^n\right\}}{\partial z} \\ \frac{1}{\rho}\frac{\partial\left\{\rho E_0\left[\left(\frac{\partial H_\rho}{\partial z} - \frac{\partial H_z}{\partial \rho}\right)/J_{c,eq}(\mathbf{H})\right]^n\right\}}{\partial \rho} \end{bmatrix} = -\mu_0\mu_r \begin{bmatrix} \frac{\partial H_\rho}{\partial t} \\ \frac{\partial H_z}{\partial t} \end{bmatrix} \tag{51}$$

(51) is the 2D governing equation that requires computation within COMSOL Multiphysics. After solving the magnetic field distribution in the numerical model, we can then obtain the current density distribution based on (47), and thus the current induced in each HTS turn is derived as

$$I_t = \iint_{S_t} \left(\frac{\partial H_\rho}{\partial z} - \frac{\partial H_z}{\partial \rho} \right) dS_t \tag{52}$$

where S_t denotes the cross-sectional area of each HTS turn.

The instantaneous power dissipation per unit volume of the coil can then be obtained as

$$P_{tot} = \sum_{j=1}^{N} E_0 \iiint_{V_j} \left[\left(\frac{\partial H_\rho}{\partial z} - \frac{\partial H_z}{\partial \rho} \right)^{n+1} / J_c^n(\mathbf{H}) \right] dV_j \tag{53}$$

where V_j is the volume of the j-th HTS turn.

In the ϕ-solved current-free region, the governing equation is written as

$$\begin{cases} \nabla \cdot \nabla \phi = 0 \\ \nabla \times (-\nabla\phi) = 0 \end{cases} \tag{54}$$

The magnetic field directly solved using the **H**-formulation and the magnetic field calculated by $-\nabla\phi$ are coupled through the boundary between the **H**-solved and ϕ-solved domains, as depicted in Fig. 3.

The numerical model implemented within COMSOL is demonstrated in Fig. 3, taking PM-1 as an example. With the exception of the double pancake HTS coil and PM sections, the remaining components are characterised by the presence of air. The establishment of the numerical model also has to take into account the setup of the moving mesh and the continuity boundary condition. The continuity boundary divides the whole model into a moving mesh region and a static domain, and the moving mesh region is defined by the deforming domain, prescribed deformation, as well as prescribed normal mesh displacement features in COMSOL. More details can be found in [40,50,51].

3.2. Experimental measurement

The experimental measurement system is shown in Fig. 4. In addition to the utilised PMs and HTS coil, the test equipment is mainly composed of a dynamometer, a current probe, an aluminum rod, and a cryogenic storage dewar. The two PMs are of the type NdFeB N50 and N52, which correspond to PM-1 and PM-2 in Table 1, respectively. The dynamometer is adopted to measure the force experienced by the tested PM, both of which are rigidly attached to one another through the aluminum rod. The double pancake HTS coil is formed by winding a single 4.2-mm-wide Bi-2223 tape without insulation. The HTS tape's ends are soldered together using a Sn-Bi alloy. Each pancake consists of 22 turns. As illustrated in Fig. 4, an extra turn has been led out to facilitate the measurement of the induced current in each turn using
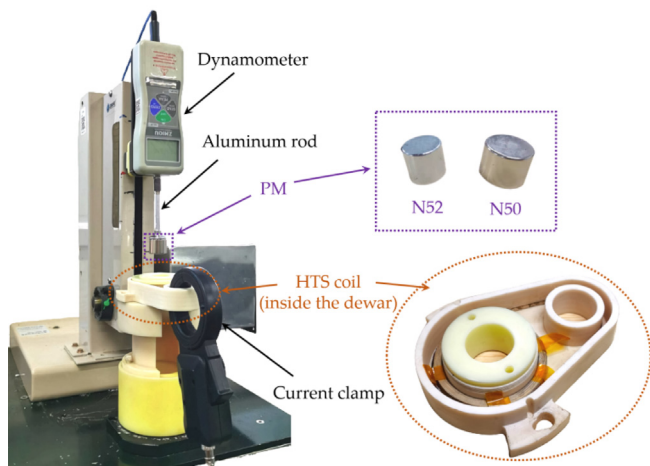

Fig. 3. The **H**-ϕ coupled numerical model of the SWE system built within COMSOL Multiphysics.

Fig. 4. Experimental setup and measurement system.

a current clamp and eliminate excess inductance disturbance from the current sensor to the tested coil. The entire double pancake HTS is placed inside the epoxy resin dewar used to hold LN₂.

At the beginning of the experiment, the PM under investigation was positioned at the center of the double pancake HTS coil, with the temperature maintained at room temperature. In this scenario, the HTS coil was not in a superconducting state. Subsequently, LN₂ was poured into the dewar to achieve 77 K enabling the HTS coil to enter the superconducting state. The motion of the PM (and the dynamometer) was controlled by a linear motor. In order to ease data collection and analysis, the velocity of the PM was set as a constant.

4. Results and analyses

Taking the double pancake Bi-2223 coil and two NdFeB PMs listed in Table 1 as the studied objects, the analytical, simulated, and measured electromechanical performances of the SWE system have been analysed in this section. The computer used for the computations is equipped with an Intel Core i7-4770 CPU running at 3.4 GHz and has 16 GB of RAM. Each **H**-ϕ formulation based numerical model in the study consists of approximately 13,250 degrees of freedom. The computation time for each model, with a relative tolerance of 10^{-3}, was approximately 13 hours. Considering the computational complexity of the numerical modelling, the simulation period has been set as 40 s.

4.1. Electromechanical characteristics

Fig. 5 and Fig. 6 show the induced total currents in the studied HTS coil, and the forces experienced by the moving PMs in the two case studies, respectively. It is easy to understand that PM-1 leads to a higher induced DC and experiences a higher mechanical force compared to the case of PM-2 because PM-1 can bring a higher initial magnetic flux to the HTS coil, which is determined by B_rV, as illustrated by Eq. (11). In general, no matter from the perspective of the induced total current or mechanical force, it can be found that the analytical results calculated by Eqs. (38) and (40) are in good accordance with the simulated results adopting the zero resistivity approximation ($\rho_{HTS} = 0$) with a deviation of less than 1%; and the experimental measurements demonstrate strong concurrence with the numerical simulation taking into account the $J_c(\mathbf{H})$ dependence, with a discrepancy of less than 4%, which meets well our expectation.

As illustrated in Section 2, the analytical equations neglect the resistance of the HTS coil, which can lead to an overestimation of both the induced current in the coil and the resulting force on the PM. As a comparison, the $J_c(\mathbf{H})$ dependence characterises better the resistivity in the HTS coil, by
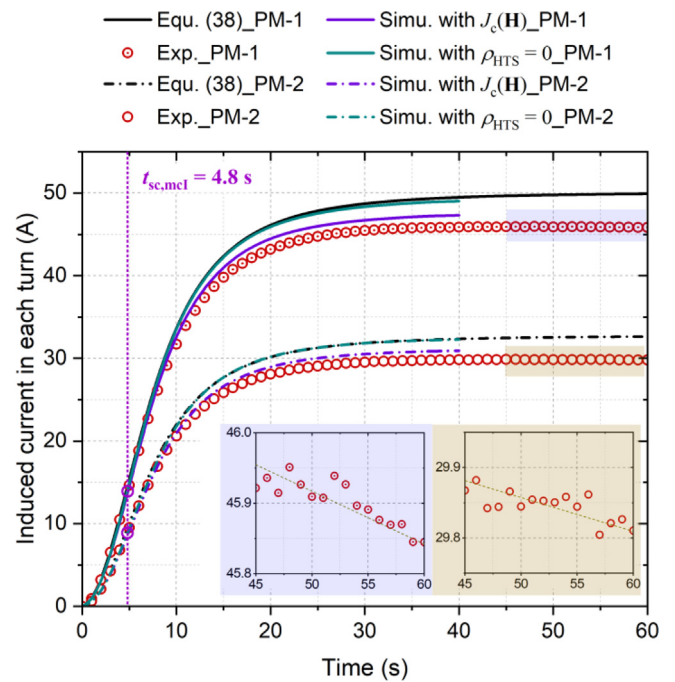

Fig. 5. Time-varying induced current within each turn of the investigated double pancake HTS coil. Equ. – Equation; Exp. – Experiment; Simu. – Simulation.
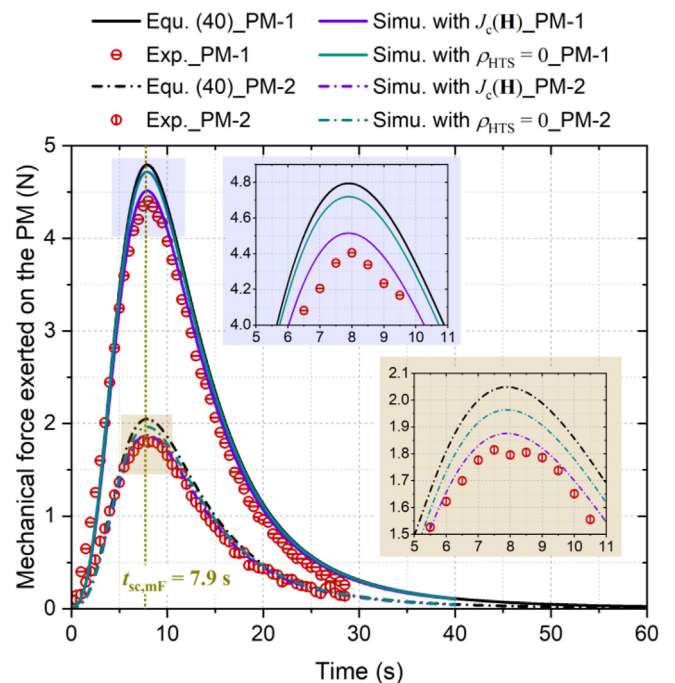

Fig. 6. Variation of the mechanical forces imparted on the studied PMs in the time domain. Equ. – Equation; Exp. – Experiment; Simu. – Simulation.

$$\rho_{HTS} = \frac{E_\varphi}{J_\varphi} = \frac{E_0}{J_{c,eq}(\mathbf{H})}\left[\frac{J_\varphi}{J_{c,eq}(\mathbf{H})}\right]^{n-1} \tag{55}$$

As a result, the numerical modelling taking into account ρ_{HTS} reflects more accurately the electromechanical behaviors of the wireless energisation system and complies better with the experimental data. Comparing the simulated and experimental results in Fig. 5, taking $t = 40$ s as an example, the induced currents in the case of PM-1 are separately 47.3

A and 45.9 A with a bias ratio of approx. 3.1%, and the induced currents in the case of PM-2 are separately 30.9 A and 29.8 A with a bias ratio of approx. of 3.7%, both of which are considered acceptable in practical applications. However, it is interesting to note that the measured currents exhibit a decaying trend for $t > 45$ s, though without a distinctive change, as shown in the subfigures of Fig. 5. In fact, as the PM is positioned at a significant distance from the HTS coil, the coil gradually transitions into the persistent current mode and thus the circulating DC should not lead to power dissipation. It is assumed that the non-superconducting Sn-Bi alloy used to join both ends of the HTS coil, which introduces a joint resistance on the order of 10^{-8} Ω, causes extra power dissipation and decreases the transport DC in the experiment. Therefore, it can be inferred that in a jointless HTS coil, e.g., a partially slit coil [52,53], the reduction of transport DC can be avoided, which deserves more investigation in the future.

In Fig. 6, it can be seen that the peak forces occur at $t = 7.9$ s, which agrees well with $t_{\text{sc,mF}}$ calculated by Eq. (23) (here $R_{\text{c,avg}}$ should be utilised). In terms of the mechanical forces experienced by the PMs, taking the case of PM-1 at $t = t_{\text{sc,mF}}$ as an example, the numerical and experimental results are 4.55 N and 4.40 N in the case of PM-1, respectively, with a bias ratio of 3.4 %, which is also considered well accepted in practice.

It has to be underlined that though the simulation exploiting the **H**-ϕ formulation and the $J_{\text{c}}(\mathbf{H})$ dependence can more accurately illustrate the electromechanical behaviors of the SWE system, it is time-consuming (approx. 13 hours in this study) to run the numerical model with acceptable accuracy. Hence, with an induced current and mechanical force bias ratio below 8%, the analytical approach outlined in Section 2 remains a valuable tool for swiftly predicting the overall performance of the entire system, prior to engaging in modeling endeavors or experimental investigations.

Considering the favorable correspondence between the experimental data and the simulated results leveraging the $J_{\text{c}}(\mathbf{H})$ dependence, the electromagnetic properties of the HTS coil have been analysed based on numerical modelling. The current density and magnetic flux density distributions across the cross section of the double pancake HTS coil are illustrated in Fig. 7, in which (a)-(d) present the magnetic flux density (B_{norm}) and current density ratio ($J_{\varphi}/J_{\text{c,eq}}$) distributions across the cross section of the double pancake HTS coil in the case of PM-1, and (e)-(h) show the case of PM-2. In general, the two cases present similar electromagnetic characteristics at the same time instant despite the differences in amplitude.

Focusing on the case of PM-1 as an illustrative example, Fig. 7(a) and (b) present the magnetic flux density and current density distributions at $t = t_{\text{sc,mcI}}$ [as illustrated in Fig. 5, calculated by Equation (22) using $R_{\text{c,avg}}$]. It can be found that at the initial stage, most of the induced current and magnetic flux are concentrated on the two edges of each turn. It is interesting to note, despite the net positive induced current, that the current direction is not unique in each turn: the distribution of the induced current is influenced by both the variation of magnetic flux in the direction of PM movement (magnetic flux density parallel to the wide surface of the HTS turn, $\boldsymbol{B_z}$) and the magnetic flux density perpendicular to the wide surface of the HTS turn ($\boldsymbol{B_\rho}$). As a result, the eddy currents due to $\boldsymbol{B_\rho}$ will enhance the induced current due to $\boldsymbol{B_z}$ on one turn edge and mitigate/surpass it on the other edge, as shown in Fig. 7(a) and (b). However, as the distance between the PM and the HTS coil increases, the influence of $\boldsymbol{B_\rho}$ becomes weaker, and so is the induced eddy current due to $\boldsymbol{B_\rho}$; hence, the current distribution at $t = 40$ s will be dominated by the induced current due to $\boldsymbol{B_z}$, as shown in Fig. 7(c) and (d). During the entire PM moving process, the magnetic flux and eddy current due to $\boldsymbol{B_\rho}$ mainly occupy the inner turns of the HTS coil, where most of the power dissipation is thus generated (detailed analyses will be presented in Section 4.2).

4.2. Power dissipation and system efficiency

The AC loss generated in the HTS coil is attributed to the external time-varying magnetic fields, and thus intuitively the magnetisation loss predominantly contributes to the overall AC loss. However, one unique feature of this SWE system is that the induced current in the HTS coil is a slowly time-varying DC, i.e., under the influence of the external fields, dynamic loss can be produced [30–32]. Therefore, the total AC power dissipation inside the HTS coil, P_{tot}, is composed of the magnetisation loss, P_{mag}, and the dynamic loss, P_{dyn}, i.e., $P_{\text{tot}} = P_{\text{mag}} + P_{\text{dyn}}$. Based on the numerical modelling results, the total dynamic power loss (W) in the HTS coil can be quantified as [43]

$$P_{\text{dyn}} = \sum_{j=1}^{N} I_j(t) \cdot \frac{1}{V_j} \iiint_V E_\varphi(t) dV_j \tag{56}$$

On the basis of (53) and (56), P_{tot}, P_{dyn}, and P_{mag} have been calculated accordingly and depicted together in Fig. 8. In general, the power dissipation is in the order of 10^{-1} mW. It can be seen that the total power dissipation is dominated by the magnetisation loss, and both the P_{tot} and P_{mag} peak values appear at approximately 4.8 s for both the PM-1 and PM-2 cases, which are in good accordance with $t_{\text{sc,mcI}}$ quantified by Eq. (22), the moment when the highest $\partial E/\partial t$ happens. In addition, although magnetisation loss constitutes a significant portion of the total AC loss, the ratio of dynamic loss to the total loss increases with time and gradually approaches a stable value, e.g., in the case of PM-1, $P_{\text{dyn}}/P_{\text{tot}}$ converges to approx. 40%. In fact, at the initial stage when the PM has not moved a significant distance away from the HTS coil, e.g., during $t < t_{\text{sc,mcI}}$, the induced DC is relatively low and thus the dynamic loss is negligible compared to the magnetisation loss. However, with the PM moving further from the HTS coil, e.g., when $t > t_{\text{sc,mF}}$, the influence of the PM field is greatly reduced and thus the magnetisation loss begins to drop. It should be noted that, given that the induced DC in the coil keeps increasing during the whole PM moving process, the ratio of dynamic loss to the total loss will keep increasing accordingly, and the dynamic loss will not reach the peak value at the same moment as the magnetisation loss. When the PM continues to move further, both the magnetisation loss and dynamic loss will keep decreasing as the PM field becomes less influential and the induced DC is approaching the persistent value. Consequently, the total AC power loss will drop to nearly zero, and $P_{\text{dyn}}/P_{\text{tot}}$ will reach a stable value given the unchanged transport DC: the variation of both the dynamic loss and magnetisation loss will be contributed purely by the PM field, which however becomes decreasingly significant.

The power loss density distribution across the cross-section of the double pancake coil is depicted in Fig. 9(a) and (b) show the loss density distributions at $t = t_{\text{sc,mcI}}$ and $t = 40$ s in the case of PM-1, respectively. Similarly, (c) and (d) separately correspond to the loss density distributions at $t = t_{\text{sc,mcI}}$ and $t = 40$ s in the case of PM-2. The two cases share the same loss density distribution pattern in spite of the difference in amplitude and thus to conduct a comprehensive analysis, the case of PM-1 will be utilised as a specific example. As seen from (a) and (b), most of the power dissipation is generated in the inner turns of the double pancake HTS coil and both edges of each turn, which complies well with Fig. 7(a)-(d). At $t = 40$ s, when the PM is sufficiently far from the HTS coil, the induced current is dominated by the transport DC due to $\boldsymbol{B_z}$ and the influence of $\boldsymbol{B_\rho}$ turns out to be negligible, therefore both the current density and loss density distributions become more even in all the turns. In addition, comparing Fig. 9 (a) and (b), it can be found that the power loss density decreases rapidly with time, which agrees well with the variation trend of P_{tot} in Fig. 8.

However, it is worth noting that the loss density distributions in the two pancakes are not always identical. Fig. 10 demonstrates the variation of the different loss components in the top and bottom pancakes of the double pancake HTS coil in the case of PM-1 in the time domain. It appears that at the initial stage, e.g., $t < 10$ s, most losses are generated in the top pancake. Given that the induced transport DC due to $\boldsymbol{B_z}$ in each turn is forced to be the same, the loss differences in the two
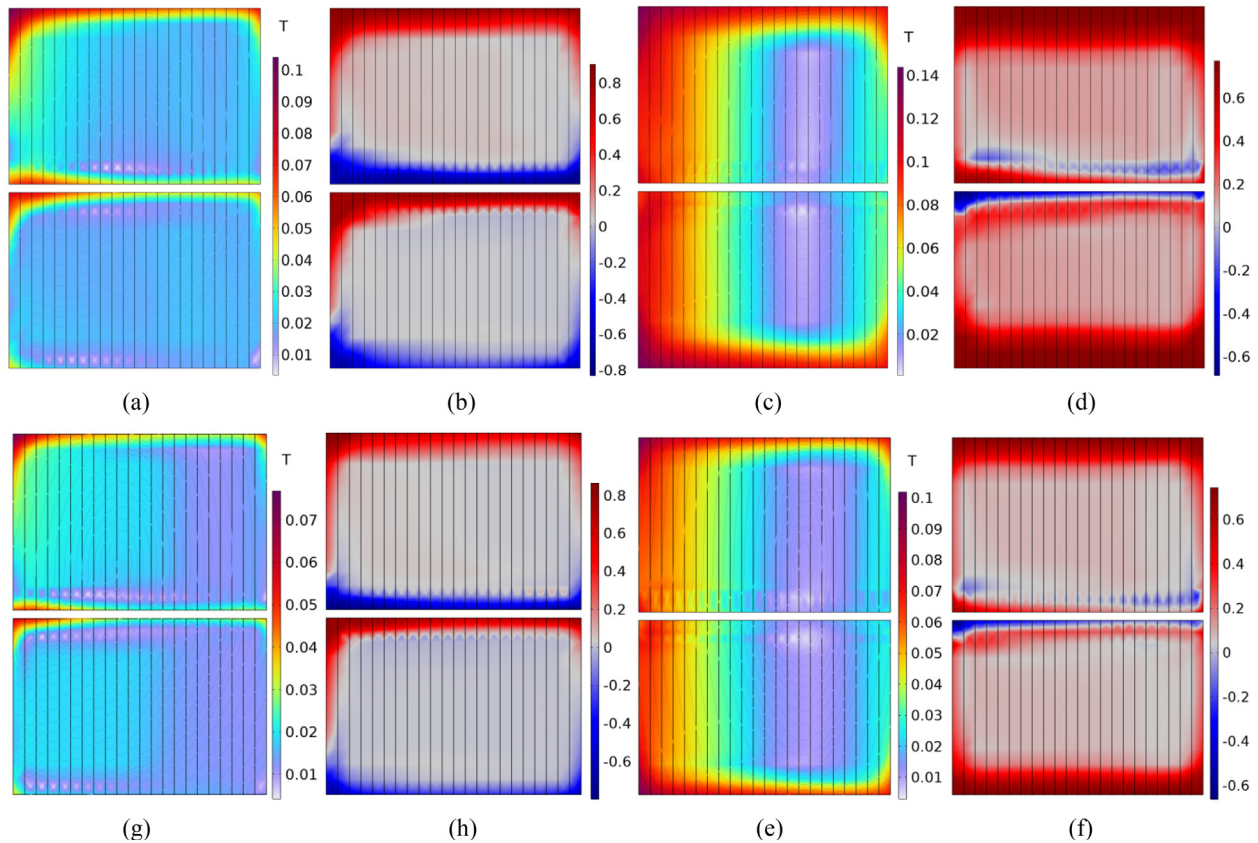
Fig. 7. Distributions of the magnetic flux density, B_{norm}, and current density ratio, $J_{\varphi}/J_{c,eq}$, across the cross section of the double pancake HTS coil. (a) and (b) depict the B_{norm} and $J_{\varphi}/J_{c,eq}$ distributions at $t = t_{sc,mcI}$ in the case of PM-1, respectively; (c) and (d) correspond to the B_{norm} and $J_{\varphi}/J_{c,eq}$ distributions at $t = 40$ s in the case of PM-1; (e) and (f) separately describe the B_{norm} and $J_{\varphi}/J_{c,eq}$ distributions at $t = t_{sc,mcI}$ in the case of PM-2; (g) and (h) illustrate the B_{norm} and $J_{\varphi}/J_{c,eq}$ distributions at $t = 40$ s in the case of PM-2.
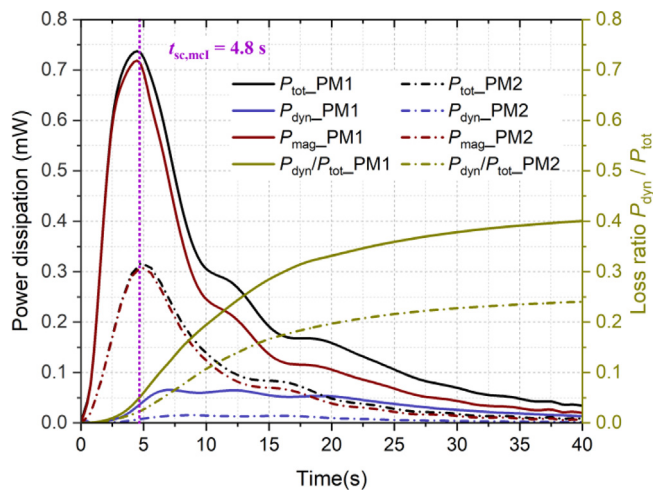

Fig. 8. Variation of the power dissipation and loss ratio in the studied double pancake HTS coil in the time domain. P_{tot} – total AC loss; P_{dyn} – dynamic loss; P_{mag} – magnetisation loss.

pancakes are caused by the variation of B_{ρ}. In fact, the PM is initially placed at the centre of the double pancake; in other words, during the entire system energisation process, the PM keeps leaving the top pancake but will go through the bottom pancake. As a result, the top pancake will experience higher B_{ρ} compared to the bottom one at the initial stage. However, with the PM moving farther from the coil

(e.g., $t > 10$ s), the bottom pancake will experience higher B_{ρ} on account of the shorter distance between it and the PM. After the integration of the total AC loss P_{tot} over the time range 40 s, the energy dissipation in the bottom pancake is 4.31 mJ, and the energy dissipation in the top pancake is 4.15 mJ. As a result, the power dissipation is generated unequally in the two pancakes and higher loss dissipation has been found in the bottom one.

According to Fig. 10, though the total AC losses, P_{tot}, for both pancakes follow a decreasing trend after $t > = t_{sc,mcI}$, it is of interest to point out that this decreasing trend is not purely monotonical, especially in the case of the bottom pancake. As far as the dynamic loss P_{dyn} is concerned, in fact, the dynamic loss in a HTS conductor is in a nonlinear positive correlation to the amplitude of the transport DC and the external magnetic field perpendicular to its wide surface [54]. During the entire PM moving process, the induced transport DC in each HTS turn keeps increasing; however, the B_{ρ} seen by the pancake coil generally keeps decreasing. Therefore, it is understandable that we can find two P_{dyn} peak values in the P_{dyn} curves: the first one is mainly contributed by a higher perpendicular field when the PM is not far enough, while the second one is caused by a higher transport DC due to the flux variation along the z-axis. Compared to the bottom pancake, at $t > 10$ s, the top pancake experiences a far lower B_{ρ} and thus its double-peak P_{dyn} effect is reasonably weaker. Additionally, considering that P_{tot} is dominated by P_{mag}, the PM keeps leaving the top pancake and the B_{ρ} acting on the top pancake keeps decreasing, and thus the total AC loss of the top pancake has a relatively monotonical decreasing trend.

Following the above analysis, the system efficiency can be quantified. Limited by the moving range of the linear motor to drive the PMs,
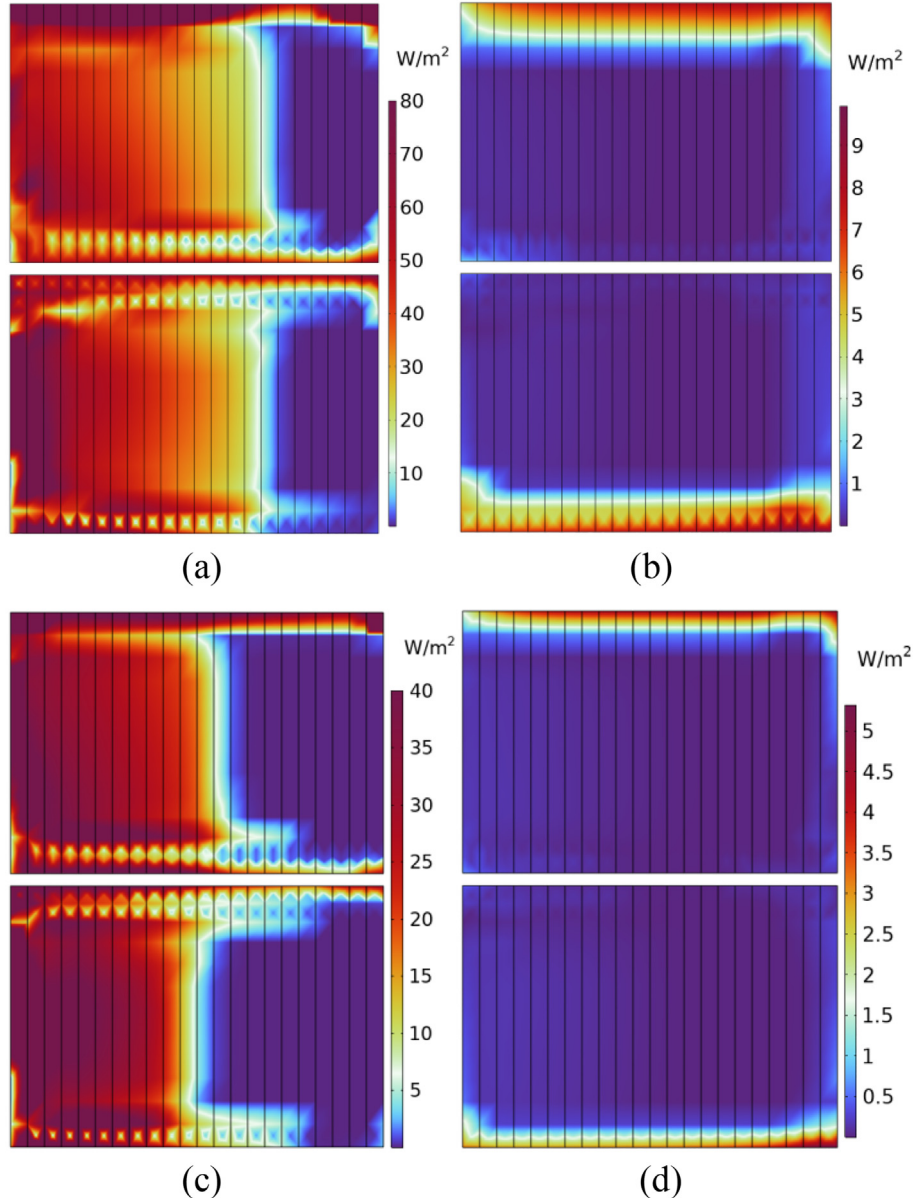
Fig. 9. Distribution of the power loss density across the cross section of the investigated HTS double pancakes. (a) and (b) present the loss density distribution at $t = t_{\mathrm{sc,mcI}}$ and $t = 40$ s in the case of PM-1, respectively; (c) and (d) separately show the loss density distribution at $t = t_{\mathrm{sc,mcI}}$ and $t = 40$ s in the case of PM-2.

we have only acquired the force data till 28.6 s, as plotted in Fig. 6. Given the good agreement between the measured forces and analytical results in Fig. 6, the force data from 28.6 to 40 s have been complemented by Eq. (40). In this way, taking PM-1 as an example, at $t = 40$ s, we have

$$
\begin{cases}
W_{\mathrm{mec,PM1}} = \int_0^{40} F_{\mathrm{tot}}(t) v \, dt = 219.88 \text{ mJ} \\
W_{\mathrm{em,PM1}} = \frac{L_{\mathrm{tot}} I_t^2(t=40)}{2} = 210.50 \text{ mJ} \\
\eta_{\mathrm{PM1}} = \frac{W_{\mathrm{em}}}{W_{\mathrm{mec}}} = 95.73 \text{ mJ}
\end{cases}
\tag{57}
$$

In the same way, the system efficiency for the case of PM-2 has been calculated as $\eta_{\mathrm{PM2}} = 96.02\%$. Therefore, it can be concluded that the overall efficiency of the tested energy conversion system at $t = 40$ s is higher than 95%. The power dissipation in the HTS coil can be obtained by

$$
W_{\mathrm{loss}} = \int_0^t P_{\mathrm{tot}}(t) \, dt
\tag{58}
$$

Based on (58) and the modelled results considering the $J_c(\mathbf{H})$ dependence, we have $W_{\mathrm{loss,PM-1}} = 8.46$ mJ, and $W_{\mathrm{loss,PM2}} = 3.24$ mJ. Therefore, compared to the electromagnetic energies stored in the HTS coil, the total AC losses of the coil during the whole energisation process appear neglectable as $W_{\mathrm{loss,PM-1}}/W_{\mathrm{mec,PM-1}} = 3.85\% < 5\%$. However, it is still of significance to consider the loss dissipated during the whole energisation process of the HTS electro-mechanical system to accurately quantify its efficiency. Additionally, an extra 0.42% of the total energy has been dissipated in the system, including the resistive loss generated in the Sn-Bi alloy coil joints, as well as other friction losses from some mechanical structures. On the other hand, it should be pointed out that the estimated $\eta_{\mathrm{PM-1}}$ and $\eta_{\mathrm{PM-2}}$ have been underestimated to some extent because we have only considered the period 0–40 s. Given that the current induced in the HTS coil keeps increasing (neglecting the influence of the non-superconducting joints) and the mechanical force experienced by the PM keeps decreasing, a longer studied period will lead to higher $W_{\mathrm{em}}/W_{\mathrm{mec}}$, and thus higher system efficiency. It is important to note that the studied SWE system
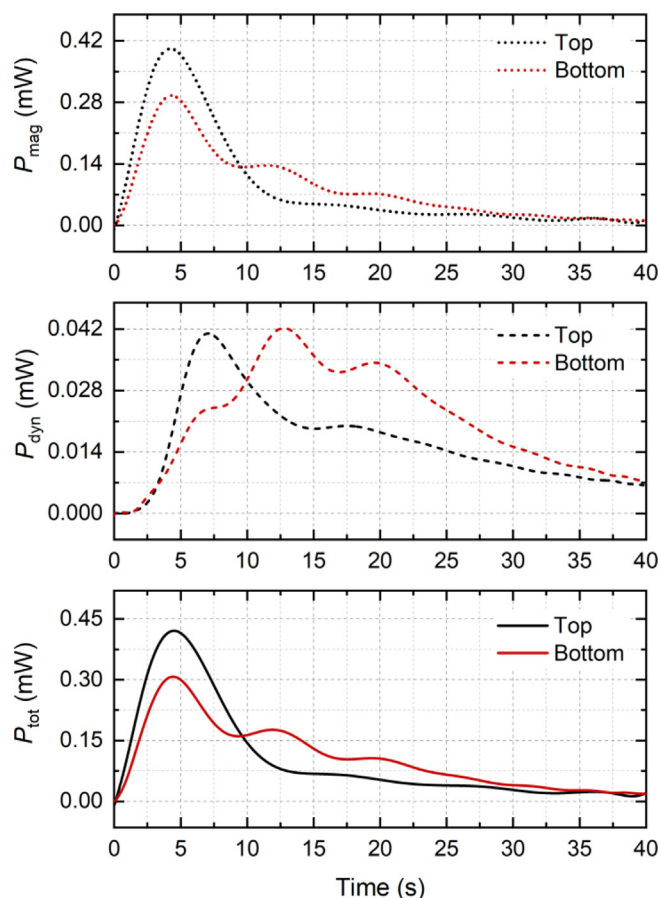
Fig. 10. Variation of the different loss components in the top and bottom pancakes of the HTS coil in the case of PM-1 in the time domain.

in the article serves as a basic device for validating the proposed wireless energization method for SMs. It is anticipated that an improved SWE system with less friction loss, equipped with a jointless SM can achieve superior system efficiency. More future research efforts are deserved.

5. Conclusions

A novel energisation method for SMs has been proposed in this paper, which leverages the principles of flux conservation and the zero DC resistivity exhibited by a superconducting circuit. A magnetic dipole, e.g., a PM, is initially put in the center of a SM, which is in the non-superconducting state (e.g., at room temperature); then, the SM is cooled below its critical temperature to achieve superconductivity, and the magnetic dipole is driven to move away from the SM. When the magnetic dipole has moved sufficiently far from the SM, a persistent DC can be induced in the SM, resulting in wireless energization of the SM.

Through theoretical analysis, numerical modelling, and experimental measurement, the proposed wireless energisation technique has been validated. The whole SWE device is essentially a highly-efficient energy conversion system. Through the utilisation of the **H**-ϕ formulation based modelling method, the power dissipation generated in the SM has been accurately calculated, which is in the order of 10^{-1} mW and is thus proven neglectable compared to the electromagnetic energy stored in the SM. Although the resistivity of the SM is neglected in the derived analytical equations, they can be conveniently exploited to estimate the electromechanical behaviors of the SWE device with a bias ratio of less than 8%, avoiding complicated and

time-consuming numerical modelling and experiments. In brief, the studied SWE equipment can achieve an overall system efficiency of no less than 95%, and it is anticipated with a jointless SM and less friction loss from the mechanical structure, superior system efficiency can be achieved.

The proposed wireless energisation method for SMs is simple and reliable. It has eliminated the heat accumulation in contact-type currents leads, the arc erosion and mechanical wear of conventional slip rings, the high costs and complex structures of inductive brushless exciters, complicated power electronics equipment, as well as long charging duration and unsatisfactory efficiency of existing superconducting flux pumps. Furthermore, dynamo-type HTS flux pumps experience reduced functionality at lower temperatures due to the escalation of the critical current, leading to an inability to generate over-critical currents effectively with the rotating magnets. As a comparison, the proposed SWE system circumvents this issue and maintains operability at lower temperatures. However, it should be noted that the success of the proposed SWE system has to rely on the achievement of the persistent current mode of the SM, i.e., a SM with extremely low resistance is the key to retaining the circulating DC. Therefore, a SWE system equipped with a jointless SM is anticipated to achieve a superior efficiency approaching 1, which deserves further research efforts in the future. It is believed that this article can help enhance the understating of the intricate electromechanical dynamics between magnetic dipoles and superconducting circuits and opens the way to step changes in future power-dense transport and energy sectors.

Declaration of Competing Interest

The authors declare that they have no known competing financial interests or personal relationships that could have appeared to influence the work reported in this paper.

References

[1] Gerbershagen A et al. The advantages and challenges of superconducting magnets in particle therapy. Supercond Sci Technol 2016;29:083001.
[2] Egorov SA, Rodin IY, Shatil NA, Zapretilina ER. Chapter 5 - superconducting magnet systems ISBN 9780081024706. In: Woodhead publishing series in energy, fundamentals of magnetic thermonuclear reactor design. Woodhead Publishing; 2018. p. 117–77. https://doi.org/10.1016/B978-0-08-102470-6.00005-6.
[3] Minervini J et al. Recent advances in superconducting magnets for MRI and hadron radiotherapy: an introduction to 'Focus on superconducting magnets for hadron therapy and MRI'. Supercond Sci Technol 2018;31:030301.
[4] Mitchell N et al. Superconductors for fusion: a roadmap. Supercond Sci Technol 2021;34:103001.
[5] Georgescu I. Superconducting accelerator technologies. Nat Rev Phys 2020;2(128).
[6] Dong F et al. An on-board 2G HTS magnets system with cooling-power-free and persistent-current operation for ultrahigh speed superconducting maglevs. Sci Rep 2019;9:11844.
[7] Bizon N. Effective mitigation of the load pulses by controlling the battery/SMES hybrid energy storage system. Appl Energy 2018;229:459–4731.
[8] Molina MG, Enrique Mercado P, Hirokazu Watanabe E. Improved superconducting magnetic energy storage (SMES) controller for high-power utility applications. IEEE Trans Energy Convers 2011;26(2):444–56.
[9] Zhu J et al. Experimental demonstration and application planning of high temperature superconducting energy storage system for renewable power grids. Appl Energy 2015;137:692–8.
[10] Li J et al. Design/test of a hybrid energy storage system for primary frequency control using a dynamic droop method in an isolated microgrid power system. Appl Energy 2017;201:257–69.
[11] Sotelo GG et al. Proposal of a novel design for linear superconducting motor using 2G tape stacks. IEEE Trans Ind Electron 2018;65(9):7477–84.

[12] Ma G-T et al. Potentials of an integrated levitation guidance and propulsion system by a superconducting transverse flux linear motor. IEEE Trans Ind Electron 2018;65(9):7548–57.

[13] Wang Y et al. Design analysis and experimental test of a segmented-rotor high-temperature superconducting flux-switching generator with stationary seal. IEEE Trans Ind Electron 2018;65(11):9047–55.

[14] Coulinge E, Burnet J, Dujic D. High-current low-voltage power supplies for superconducting magnets. In: 2017 International Symposium on Power Electronics (Ee). p. 1–6. https://doi.org/10.1109/PEE.2017.8171666.

[15] Qu R et al. Review of superconducting generator topologies for direct-drive wind turbines. IEEE Trans Appl Supercond 2013;23(3). 5201108–5201108.

[16] Tang J et al. Modeling and experimental verification of high-frequency inductive brushless exciter for electrically excited synchronous machines. IEEE Trans Ind Appl 2019;55(5):4613–23.

[17] Jiao N et al. Design and control of a two-phase brushless exciter for aircraft wound-rotor synchronous starter/generator in the starting mode. IEEE Trans Power Electron 2016;31(6):4452–61.

[18] Amada Y et al. Study on V-I characteristic in natural graphite brush vs steel slip ring system. In: 2018 IEEE Holm Conference on Electrical Contacts. p. 393–8. https://doi.org/10.1109/HOLM.2018.8611636.

[19] Basu Swapan, Debnath Ajay Kumar. Chapter 9 - Turbo generator control system, power plant instrumentation and control handbook. second ed. Academic Press; 2019, p. 743–96, ISBN 9780128195048, https://doi.org/10.1016/B978-0-12-819504-8.00009-3.

[20] Bumby CW et al. Development of a brushless HTS exciter for a 10 kW HTS synchronous generator. Supercond Sci Technol 2016;29:024008.

[21] Chen H, Zhang H. AC loss mitigation for high temperature superconducting coils in wireless power transfer. Superconductivity 2023;6:100044.

[22] Wen Z et al. A statistical model for the design of rotary HTS flux pumps based on deep-learning neuron network. Superconductivity 2022;3:100017.

[23] Coombs TA. Superconducting flux pumps. J Appl Phys 2019;125:230902.

[24] Wen Z et al. High Temperature Superconducting Flux Pumps for Contactless Energization. Crystals 2022;12(6):766.

[25] van de Klundert LJM, ten Kate HHJ. Fully superconducting rectifiers and flux pumps. Part 1: Realized methods for pumping flux. Cryogenics 1981;21 (4):195–206.

[26] van de Klundert LJM, ten Kate HHJ. On fully superconducting rectifiers and flux pumps. Part 2: Commutation modes characteristics and switches. Cryogenics 1981;21(5):267–77.

[27] Coombs TA, Geng J, Fu L, Matsuda K. An overview of flux pumps for HTS coils. IEEE Trans Appl Supercond 2017;27(4):1–6.

[28] Mataira RC et al. Origin of the DC output voltage from a high-T_c superconducting dynamo. Appl Phys Lett 2019;114:162601.

[29] Geng J et al. Origin of DC voltage in type II superconducting flux pumps: Field, field rate of change, and current density dependence of resistivity. J Phys D Appl Phys 2016;49:11LT01.

[30] Jiang Z et al. Dynamic resistance of a high-T_c superconducting flux pump. Appl Phys Lett 2014;105:112601.

[31] Zhang H et al. Demarcation currents and corner field for dynamic resistance of HTS-coated conductors. IEEE Trans Appl Supercond 2020;30(8):1–5.

[32] Jiang Z et al. Dynamic resistance of a high-T_c coated conductor wire in a perpendicular magnetic field at 77 K. Supercond Sci Technol 2017;30(3):pp. 03LT01.

[33] Zhang H et al. A full-range formulation for dynamic loss of high-temperature superconductor coated conductors. Supercond Sci Technol 2020;33:05LT01.

[34] Zhang H et al. Dependence of dynamic loss on critical current and n-value of HTS coated conductors. IEEE Trans Appl Supercond 2019;29(8):1–7.

[35] Zhang H et al. Alternating current loss of superconductors applied to superconducting electrical machines. Energies 2021;14(8):2234.

[36] Geng J, Badcock RA, Bumby CW. A wireless rectifier for inductively energizing high direct-current high-temperature superconducting magnets. IEEE Trans Ind Electron 2021;68(4):3273–81.

[37] Xin Y et al. Superconductors and Lenz's law. Supercond Sci Technol 2020;33:055004.

[38] Li C et al. Mechanism of a novel mechanically operated contactless HTS energy converter. Energy 2022;241:122832.

[39] Li W et al. Experimental study of a novel superconducting energy conversion storage device. Energ Conver Manage 2021;243:114350.

[40] Zhang H et al. Origin of the anomalous electromechanical interaction between a moving magnetic dipole and a closed superconducting loop. Supercond Sci Technol 2022;35(4):045009.

[41] Jackson JD. Classical electrodynamics. 3rd ed. New York: Wiley; 1998. p. 181–8. ISBN 978-0-471-30932-1.

[42] Zhang H et al. Modelling of electromagnetic loss in HTS coated conductors over a wide frequency band. Supercond Sci Technol 2020;33(2):025004.

[43] Zhang H et al. Dynamic loss and magnetization loss of HTS coated conductors, stacks, and coils for high-speed synchronous machines. Supercond Sci Technol 2020;33(8):084008.

[44] Zhang H et al. Electromagnetic properties of curved HTS trapped field stacks under high-frequency cross fields for high-speed rotating machines. Supercond Sci Technol 2021;34(4):045018.

[45] Arsenault A et al. Implementation of the H-ϕ formulation in COMSOL multiphysics for simulating the magnetization of bulk superconductors and comparison With the H-formulation. IEEE Trans Appl Supercond 2021;31(2):1–11.

[46] Rhyner J. Magnetic properties and AC-losses of superconductors with power law current—voltage characteristics. Physica C 1993;212:292–300.

[47] Gömöry F. Improvement of the self-field critical current of a high-Tc superconducting tape by the edge cover from soft ferromagnetic material. Appl Phys Lett 2006;89:072506.

[48] Zermeno VMR, Grilli F. 3D modeling and simulation of 2G HTS stacks and coils. Supercond Sci Technol 2014;27:044025.

[49] Zermeno VMR et al. Calculation of alternating current losses in stacks and coils made of second generation high temperature superconducting tapes for large scale applications. J Appl Phys 2013;114:173901.

[50] Li G et al. Dynamic modelling methodology for an HTS energy converter using moving mesh. Supercond Sci Technol 2021;34:105006.

[51] Grilli F et al. Dynamic modelling methodology for an HTS energy converter using moving mesh. Supercond Sci Technol 2018;31(12):125003.

[52] Lee H-G et al. Design and fabrication of permanent mode magnet by using coated conductor. Physica C 2006;445–448:1099–102.

[53] Levin GA et al. Persistent current in coils made out of second generation high temperature superconductor wire. Appl Phys Lett 2008;93:062504.

[54] Zhang H et al. Dynamic resistance and dynamic loss in a ReBCO superconductor. Supercond Sci Technol 2022;35(11):113001.